

## AUTHOR QUERY FORM

	<p>Journal: Rev. Sci. Instrum.</p> <p>Article Number: RSI23-AR-02281</p>	<p>Please provide your responses and any corrections by annotating this PDF and uploading it to AIP's eProof website as detailed in the Welcome email.</p>
---	--	--

Dear Author,

Below are the queries associated with your article. Please answer all of these queries before sending the proof back to AIP.

**Article checklist:** In order to ensure greater accuracy, please check the following and make all necessary corrections before returning your proof.

1. Is the title of your article accurate and spelled correctly?
2. Please check affiliations including spelling, completeness, and correct linking to authors.
3. Did you remember to include acknowledgment of funding, if required, and is it accurate?

Location in article	Query/Remark: click on the Q link to navigate to the appropriate spot in the proof. There, insert your comments as a PDF annotation.
<a href="#">Q1</a>	Please check that the author names are in the proper order and spelled correctly. Also, please ensure that each author's given and surnames have been correctly identified (given names are highlighted in red and surnames appear in blue).
<a href="#">Q2</a>	In the text, all the variables are italic in some places; roman in others. Please check and change if you would like them to be set consistently throughout your paper.
<a href="#">Q3</a>	Please confirm the change in page number in Refs. 1, 19, 42, and 46.
<a href="#">Q4</a>	Please provide author's group, publisher's name, and year of publication in Ref. 12.
<a href="#">Q5</a>	Please confirm the change in volume number in Ref. 17.
<a href="#">Q6</a>	Please confirm the content in Refs. 24, 36, and 44, as we have inserted the required information.  Please confirm ORCIDs are accurate. If you wish to add an ORCID for any author that does not have one, you may do so now. For more information on ORCID, see <a href="https://orcid.org/">https://orcid.org/</a> .  <a href="#">A. Devitre</a> – 0000-0001-7428-0373 <a href="#">D. X. Fischer</a> – 0000-0003-2916-8555 <a href="#">K. B. Woller</a> – 0000-0002-0450-9731 <a href="#">B. C. Clark</a> – 0009-0001-0064-4290 <a href="#">M. P. Short</a> – 0000-0002-9216-2482 <a href="#">D. G. Whyte</a> – 0000-0002-9001-5606 <a href="#">Z. S. Hartwig</a> – 0000-0003-4248-7876

Thank you for your assistance.

# A facility for cryogenic ion irradiation and *in situ* characterization of rare-earth barium copper oxide superconducting tapes

Cite as: Rev. Sci. Instrum. 95, 000000 (2024); doi: 10.1063/5.0200936

Submitted: 29 January 2024 • Accepted: 3 June 2024 •

Published Online: 9 99 9999



View Online



Export Citation



CrossMark

Q1

A. Devitre,<sup>a)</sup> D. X. Fischer,<sup>b)</sup> K. B. Woller, B. C. Clark, M. P. Short, D. G. Whyte, and Z. S. Hartwig

## AFFILIATIONS

Plasma Science and Fusion Center, Massachusetts Institute of Technology Cambridge, Massachusetts 02139, USA

<sup>a)</sup>Author to whom correspondence should be addressed: devitre@mit.edu

<sup>b)</sup>dafisch@mit.edu

## ABSTRACT

Superconducting magnets based on Rare Earth Barium Copper Oxides (REBCO) offer transformative capabilities in the fields of fusion energy, high energy physics, and space exploration. A challenge shared by these applications is the limited lifetime of REBCO due to radiation damage sustained during operation. Here we present a new ion-beam facility that enables simultaneous cryogenic irradiation and *in situ* characterization of commercial REBCO tapes. The ion source provides spatially uniform fluxes up to  $10^{19}$  protons/m<sup>2</sup>s with kinetic energies up to 3.4 MeV, in addition to helium and higher-Z species. Using this facility, we can induce uniform damage profiles in the first 10–20 μm of REBCO tapes with less than 0.25 appm of hydrogen implanted in REBCO after a dose of  $10^{20}$  protons/m<sup>2</sup>. The tape can be held at 20–300 K with an accuracy of ±0.1 K and is connected to a four-point probe measuring the critical current,  $I_c$ , and critical temperature,  $T_c$ , before, during, and after irradiation with transport current ranging from 100 nA to 100 A and a typical voltage noise less than 0.1 μV. These capabilities are presently used to study the effect of irradiation temperature on REBCO performance change during and after proton bombardment, to assess the possibility of  $I_c$  and  $T_c$  recovery after irradiation through thermal annealing, and to explore the instantaneous and recoverable suppression of  $I_c$  and  $T_c$  observed during irradiation.

© 2024 Author(s). All article content, except where otherwise noted, is licensed under a Creative Commons Attribution (CC BY) license (<https://creativecommons.org/licenses/by/4.0/>). <https://doi.org/10.1063/5.0200936>

## I. INTRODUCTION

Large-scale superconducting magnets have been an important enabling technology in science and industry since the 1960s, when low temperature superconductors like NbTi and Nb<sub>3</sub>Sn began displacing resistive copper magnets in a number of applications such as medical imaging, particle accelerators, and fusion energy devices. The advantages of superconducting magnets in these applications are twofold: first, significantly lower power consumption, which reduces operating costs; and second, access to much higher magnetic fields, which opens up new scientific and practical capabilities. The discovery and industrial production<sup>1</sup> of rare earth barium copper oxides (REBCO) have enabled research and development toward a new generation of large-scale magnets operating well in excess of 15 T. The impacts of such magnets on the fields of fusion energy,

high energy physics (HEP), nuclear medicine, and space applications, in particular, are transformative. For magnetic-fusion devices, key performance metrics scale non-linearly with the magnetic field,  $B$ , confining the thermonuclear plasma. For example, the tokamak's fusion power density scales like  $B^4$ , which provides the ability to dramatically reduce the size, cost, and time-to-build fusion power plants by using high-field REBCO magnets.<sup>2</sup> Favorable scalings coupled to the maturation of REBCO-magnet technology have led recent efforts to accelerate the commercialization of fusion energy by integrating high-field REBCO magnets into compact fusion energy devices such as tokamaks,<sup>3,4</sup> stellarators,<sup>5</sup> and magnetic mirrors.<sup>6</sup> Similarly, in HEP experiments, increasing the magnetic field plays a pivotal role in reducing the diameter of the collider ring. In order to expand the energy frontier beyond the 14 TeV available at CERN's Large Hadron Collider, increasingly higher magnetic fields

will be required to enable practical costs, siting, and construction of such devices. For aerospace applications, the ability to produce high magnetic fields at low power and small mass enables new concepts for radiation shielding of astronauts and electronics,<sup>7</sup> lunar magnetic energy storage in permanently shadowed regions,<sup>8</sup> and long-lived, enhanced-maneuverability thrusters for satellites and deep-space.

A common unifying theme for these applications is that the superconductor is exposed to ionizing radiation fields during operation. Over prolonged periods of time, microstructural changes induced by radiation damage degrade the ability of the magnet to carry current without resistance and, hence, its ability to produce the desired magnetic field. Strategies for mitigation are expensive and time-consuming, requiring costly upfront design and fabrication decisions or wholesale replacement of the magnets. For example, conceptual design studies of future fusion energy power plants<sup>9</sup> and next-generation colliders<sup>10</sup> identify superconducting magnets as the dominant technical cost and schedule driver for new facilities. Therefore, understanding the radiation tolerance of magnets in these machines becomes necessary for proper design, accurate costing, and successful operation.

In these devices, magnets operate under a complex set of physical conditions, each of which can influence the response of REBCO to radiation. These include cryogenic temperatures, immersion in a high magnetic field, and the transport of electrical current. Due to the challenge of replicating these conditions within a laboratory-based radiation facility, almost all data on radiation damage in commercial REBCO coated conductors has been acquired following irradiation at or above room temperature ( $T_{\text{irr}} \geq 293$  K), ~~in self-field ( $B = 0$  T)~~, and without transport current, leaving large uncertainties about how these results translate to the operation of REBCO under irradiation at 4–20 K in a 10–20 T magnetic field.

To address this shortcoming, we have developed an ion-beam facility for the irradiation of REBCO coated conductors at cryogenic temperatures, imparting the ability to measure the superconducting properties before, during, and after irradiation. We describe the major elements of this facility and present a series of initial test results. These data validate the capabilities of our facility and reveal a thermal-annealing recovery of the superconducting properties starting well below room-temperature.

## II. RADIATION DAMAGE IN REBCO

### A. A short review of superconductivity

Superconductivity is a thermodynamic state characterized by positive interactions between electrons (Cooper pairs), enabling near-zero electrical resistance.<sup>11,12</sup> Cooper-pairs form when temperature drops below the critical temperature,  $T_c$ , and break if the ambient magnetic field is too high. The loss-free transport of current in technical superconductors is based on a phenomenon called flux pinning.<sup>13</sup> Above the lower critical field  $H_{c1}$ , magnetic flux enters the bulk of the material as vortices, consisting of normal-conducting cores surrounded by screening currents. Consequently, any applied transport current,  $I_{\text{op}}$ , flowing through the material causes a Lorentz force,  $F_l \propto I_{\text{op}} \times B$ , acting on the vortices. Below a certain critical current,  $I_c$ , the Lorentz force is counteracted by the pinning force  $F_p$ , arising from spatial variations in Cooper pair density (or pinning

potential) within the unit cell or at lattice defects. Above  $I_c$ ,  $F_l > F_p$ ; the vortices are no longer pinned and start moving. An electric field appears, causing electrical resistance. The relationship between the emerging electric field,  $E$ , and  $I_{\text{op}}$  can be described by a power law

$$E(I_{\text{op}}) = E_c \left( \frac{I_{\text{op}}}{I_c} \right)^n, \quad (1)$$

which defines  $I_c$  through the conventional<sup>14</sup> electric-field criterion  $E_c = 1 \mu\text{V}/\text{cm}$ . The exponent,  $n$ , describes the sharpness of the transition from the loss-free to the resistive state. While the mechanism for Cooper pair formation in the cuprates remains a mystery,<sup>12</sup> radiation has been used to modify the pinning landscape of superconductors and evaluate the consequences of different microstructures on superconductivity.<sup>15</sup>

### B. Radiation-induced defects in REBCO

There is a large body of literature on the irradiation of REBCO with gamma photons,<sup>16</sup> electrons,<sup>17</sup> neutrons,<sup>18</sup> protons,<sup>9</sup> and heavy ions.<sup>19</sup> Gamma and other photon irradiations have repeatedly shown little to no effect on the superconducting properties, including recent cryogenic-irradiations with *in situ* transport measurements.<sup>16</sup> While electrons at MeV energies only produce isolated vacancy-interstitial pairs, neutrons and ions can also create collision cascades, clusters, and amorphized tracks.<sup>20</sup>

The larger defects have long been observed with transmission electron microscopy (TEM).<sup>21</sup> Most recently, Linden *et al.*<sup>22</sup> imaged the REBCO layer of coated-conductors irradiated in a fission reactor-core, where the thermal neutron spectrum was shielded by a cadmium foil. They found evidence of collision cascades in the form of 2–3 nm amorphous regions surrounded by a strain field about double the size. These large defects were stable up to 575 K.

Point defects, on the other hand, have not been observed directly. Their presence can be inferred, as we will show, from the recovery of  $I_c$  and  $T_c$  observed after annealing in cryogenically irradiated tapes. With prolonged irradiation, the accumulation of point defects and small clusters reduces  $T_c$  by scattering superconducting charge carriers. However, the mechanism for  $I_c$  degradation is not well understood: a moderate increase in the defect density can enhance  $I_c$ —especially in an external magnetic field—by improving flux pinning, but large defect concentrations will decrease  $I_c$ ,<sup>18</sup> likely due to a decreasing Cooper pair density.<sup>15</sup>

Unraveling the structure-to-property relation requires the characterization of radiation-induced pinning-landscapes and their effect on superconducting properties. The first step is to develop a facility to irradiate and measure the properties of REBCO tapes at cryogenic temperatures, with the option to apply an external magnetic field. From there, microstructural analysis tools should be added to identify the relevant defects and quantify their accumulation in magnet-operating conditions. For example, the irradiated REBCO tapes could be transferred in liquid nitrogen to an advanced electron microscope with sufficient resolution to resolve the structure of the oxygen sub-lattice<sup>23</sup> or to a synchrotron for chemical analysis.<sup>24</sup> The size distribution and concentration of open-volume defects, as well as their location within the unit cell, could be determined with a slow-positron beam equipped with lifetime and Doppler-broadening detectors.<sup>25,26</sup> Such a device, coupled to a cryogenic irradiation target capable of measuring  $I_c$ ,  $T_c$ , and the

166 density of charge carriers *in situ*, would provide a direct relation  
167 between microstructural changes and the performance degradation  
168 of REBCO tapes.

### 169 C. Existing facilities for the irradiation of coated 170 superconductors at cryogenic temperatures

171 An ideal facility to explore radiation effects in superconducting  
172 REBCO magnets should have the ability to directly characterize  
173  $I_c$  and  $T_c$  at relevant magnet operating temperatures and mag-  
174 netic fields (magnitude and direction). The nature of the incident  
175 particles and their energy spectrum should match the conditions  
176 of the application. The achievable dose should be commensurate  
177 with the expected lifetime of the magnet. The capability to mea-  
178 sure  $I_c$  and  $T_c$  *in situ* while maintaining cryogenic temperatures  
179 between irradiation and measurement is necessary to capture the  
180 evolution of an irradiated magnet during long-periods of opera-  
181 tion and isolate the effect of magnet warm-up during maintenance.  
182 The capability to measure  $I_c$  and  $T_c$  *in operando*—with transporting  
183 current during irradiation—is essential to characterize the behavior  
184 of the superconductor during operation. Historically, few exper-  
185 iments have incorporated all of these capabilities at once. Here, we  
186 review two classes of such facilities: neutron irradiation in or next  
187 to experimental fission reactors; and charged particle irradiation on  
188 accelerator beamlines.

189 Fission reactor<sup>27</sup> and spallation<sup>28</sup> neutron irradiation present  
190 two main challenges: the first is a mismatch between the interme-  
191 diate energies present in fusion or HEP magnets and the slow-to-  
192 thermal (fission) or very fast (spallation) neutron energy spectra.  
193 The second relates to space and regulatory constraints, as well  
194 as high nuclear and conductive loads. Despite these challenges,  
195 cryogenic neutron irradiation of thin REBCO films and bulk spec-  
196 iments was performed at three facilities in the late 1980s and early  
197 1990s. The low-temperature irradiation loop at Kyoto University<sup>29</sup>  
198 was used to irradiate REBCO at 20 K up to a dose of  $2 \times 10^{20}$   
199 neutrons/m<sup>2</sup>, too low to observe any change in  $T_c$ . Researchers at  
200 the Munich research reactor<sup>30,31</sup> achieved a much higher fast neu-  
201 tron fluence of  $9 \times 10^{22}$  n/m<sup>2</sup> at 15 K. They observed about 50%  $T_c$   
202 degradation but did not publish annealing data. A team at the Insti-  
203 tute for Metal Physics in Russia<sup>32</sup> irradiated REBCO at 80 K up to  
204  $10^{23}$  n/m<sup>2</sup>. They did not measure  $T_c$  *in situ*, but they observed an  
205 additional recovery of  $T_c$  after 2 weeks at 300 K, compared to  $T_c$   
206 measured 20 min after warm-up. To our knowledge, there was only  
207 one successful cold sample transfer<sup>33</sup> to an external measurement  
208 setup ( $T < 77$  K) following a cryogenic irradiation ( $T \sim 4.6$  K). It  
209 revealed changes in  $I_c$  as a function of temperature and magnetic  
210 field up to 8 T.

211 In contrast to neutron experiments, charged particle facilities  
212 offer significant flexibility, particularly for the implementation of a  
213 cryogenic irradiation target. Here, the challenge is to maintain excel-  
214 lent temperature control of the samples during irradiation through  
215 careful engineering of the target holder. For instance, Coulomb col-  
216 lisions between incident ions and lattice atoms can cause local heating  
217 in the superconducting layer up to several GW/m<sup>3</sup>. Researchers at  
218 the Karlsruhe Institute of Technology irradiated REBCO thin-films  
219 as early as the late 1980s. These 800 nm thick films were irradiated at  
220 77 K with 300 keV He to a fluence of  $2 \times 10^{20}$  ions/m<sup>2</sup>, which com-  
221 pletely amorphized the lattice structure.<sup>34</sup> More recently, in 2017,

Sorbom irradiated commercial REBCO tapes with protons at 80,  
323 and 423 K. These experiments identified differences in degrada-  
223 tion rate and field-angle dependence of  $I_c$  as a function of irradiation  
224 temperature.<sup>35</sup> The ion irradiation experiment presented in this  
225 article extends the capabilities developed by Sorbom. First commis-  
226 sioned in January 2020, this new facility allows (i) a gradual increase  
227 in sample temperature after irradiation; (ii) the measurement of  $I_c$   
228 and  $T_c$  during irradiation; and (iii) the use of different ion-beam  
229 species. A comparable setup has been developed and operated at the  
230 Surrey ion-beam laboratory in the UK.<sup>36</sup>

## 232 III. EXPERIMENTAL EQUIPMENT AND METHODS

### 233 A. REBCO coated-conductor samples

234 Coated conductors, also known as “tapes,” are materials of  
235 various layer-thicknesses and compositions. Figure 1, for example,  
236 shows the tape composition of Faraday Factory Japan:<sup>1</sup> 2  $\mu\text{m}$  of  
237 YBCO with dispersed  $\text{Y}_2\text{O}_3$  nanoparticles capped by 2  $\mu\text{m}$  of silver.  
238 A Hastelloy substrate ( $38 \pm 3 \mu\text{m}$ ) provides mechanical stability over  
239 the wide range of temperatures experienced by the tape. The buffer  
240 facilitates the bi-axial growth of the REBCO layer, warranting low  
241 angles between grains and allowing high critical currents.<sup>37</sup> Off-the-  
242 shelf tapes also include a copper jacket surrounding the stack to help  
243 with temperature stability and current distribution in cables. How-  
244 ever, our tapes were procured without a stabilizer, such that light  
245 ions with single MeV energies can produce a uniform damage profile  
246 in the REBCO layer and implant several microns into the substrate.

247 The cryogenic target holder accommodates 3–6 cm long sam-  
248 ples of REBCO tape, compatible with the magnet bore diameter  
249 of many high-field characterization facilities.<sup>15,38</sup> Halfway along the  
250 tape, the 4 mm width is reduced to a 0.1 mm bridge; the silver,  
251 REBCO, and buffers are ablated on both sides of the bridge, leav-  
252 ing the substrate exposed. ~~The bridging tape~~ has several advantages,  
253 as follows:

- 40× less transport current needed to measure  $I_c$ .
- Lower transport currents cause less Joule heating  $\propto I^2$ .
- A bridge length  $l = 2$  mm yields a well-defined voltage  
criterion  $V(I_c) = V_c = E_{cl} = 0.2 \mu\text{V}$ .
- The properties of the tape are determined by the bridge,  
which reduces the beam spot size needed to irradiate  
homogeneously and allows for higher ion fluxes.

254 Custom bridge patterns are programmed in the SCAPS SAM-  
255 Light control software and engraved by a Bright Solutions Wedge  
256 XF 532 OEM Integrated Marker, operating at 80 W and 50 kHz,  
257 scanning at a speed of 200 mm/s. A recent Master’s thesis com-  
258 pares the laser-skiving technique to the more common chemical  
259 etching and photolithographic processes. Several bridge patterns  
260 were tested between 4 and 77.3 K in magnetic fields up to 20 T,  
261 finding that microbridges with widths ranging from 40 to 400  
262  $\mu\text{m}$  retained a larger fraction of the full tape  $n$ -value and criti-  
263 cal current as compared to chemically etched bridges of the same  
264 width.<sup>39</sup>

### 265 B. Ion accelerator, beamline, and irradiation chamber

266 The ion source is a General Ionix 1.7 MV tandem accelerator  
267 operated at the MIT CLASS accelerator laboratory. The accelerator  
268

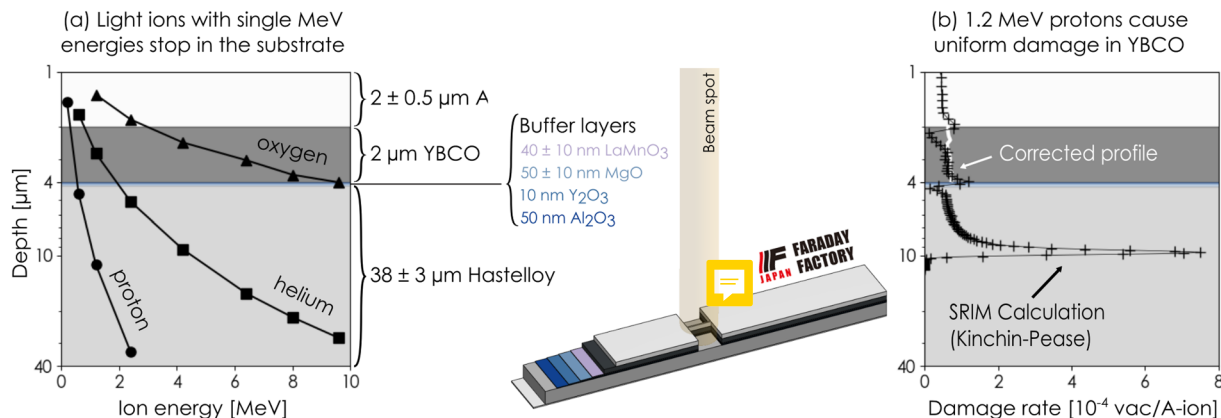


FIG. 1. Calculations of ion implantation depth and the damage profile caused by light ions with single MeV energies show that there is (a) little to no implantation of protons in the REBCO layer and (b) a uniform, neutron-like damage profile.

provides proton beam currents ranging from a few nA up to tens of  $\mu$ A, which can be kept within  $\pm 1\%$  for several hours of irradiation. This allows a uniform beam current density of up to  $10^{19}$  ions/m<sup>2</sup>s on the sample. The ion beam is extracted from the accelerator column and magnetically steered onto the target holder, attached to the cold head, at the end of the beamline. The beamline, shown in Fig. 2, contains instrumentation and diagnostics to measure the beam current and maintain its spatial uniformity. An upstream quadrupole magnet shapes the beam into a Gaussian profile, with a FWHM larger than the aperture of the collimator. This provision constrains flux uniformity (dose rate) to a factor of two. While the results presented below use 1.2 MeV protons as a proxy for fusion neutrons at the magnets of an ARC-class reactor,<sup>9</sup> the ion source can produce a variety of light and heavy ions, including He, O, Si, and most transition metals. The maximum kinetic energy of a given ion-beam species  $E_{beam} = 2qV_{ter} + V_{ext}$  depends on its charge-state, q, the source extraction voltage,  $V_{ext}$ , and the terminal potential  $V_{ter}$ . The value of  $V_{ter}$  and, therefore,  $E_{beam}$  is known with a precision of  $\pm 5$  kV. Meanwhile, the maximum achievable beam current depends on the production of the desired ion charge state by charge-exchange at the terminal, where negatively charged ions are stripped of their electrons by nitrogen gas.

### C. Target holder design and implementation

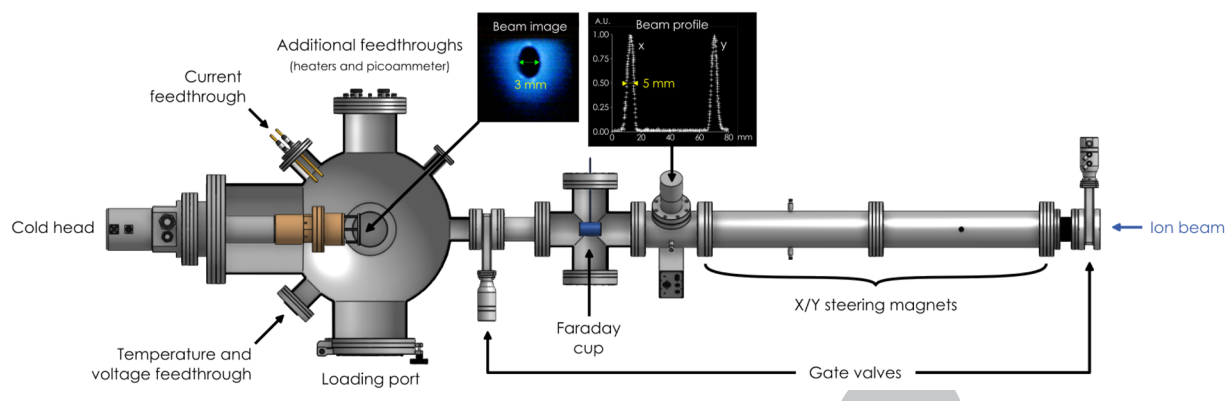
The cryogenic target holder, shown in Fig. 3, is assembled outside the irradiation chamber and attached to the cold head via mounting screws. Its design fulfills, in particular, three major requirements as follows:

1. Temperature control between 20 and  $300 \pm 0.1$  K.
2. Uniform irradiation of the REBCO layer, with a flux uncertainty less than  $1 \text{ nA} \sim 10^{15} \text{ protons/m}^2\text{s}$ .
3. Measurement of  $I_c$  and  $T_c$  during and after irradiation with a voltage noise level  $\delta V \leq 0.1 \mu\text{V}$ .

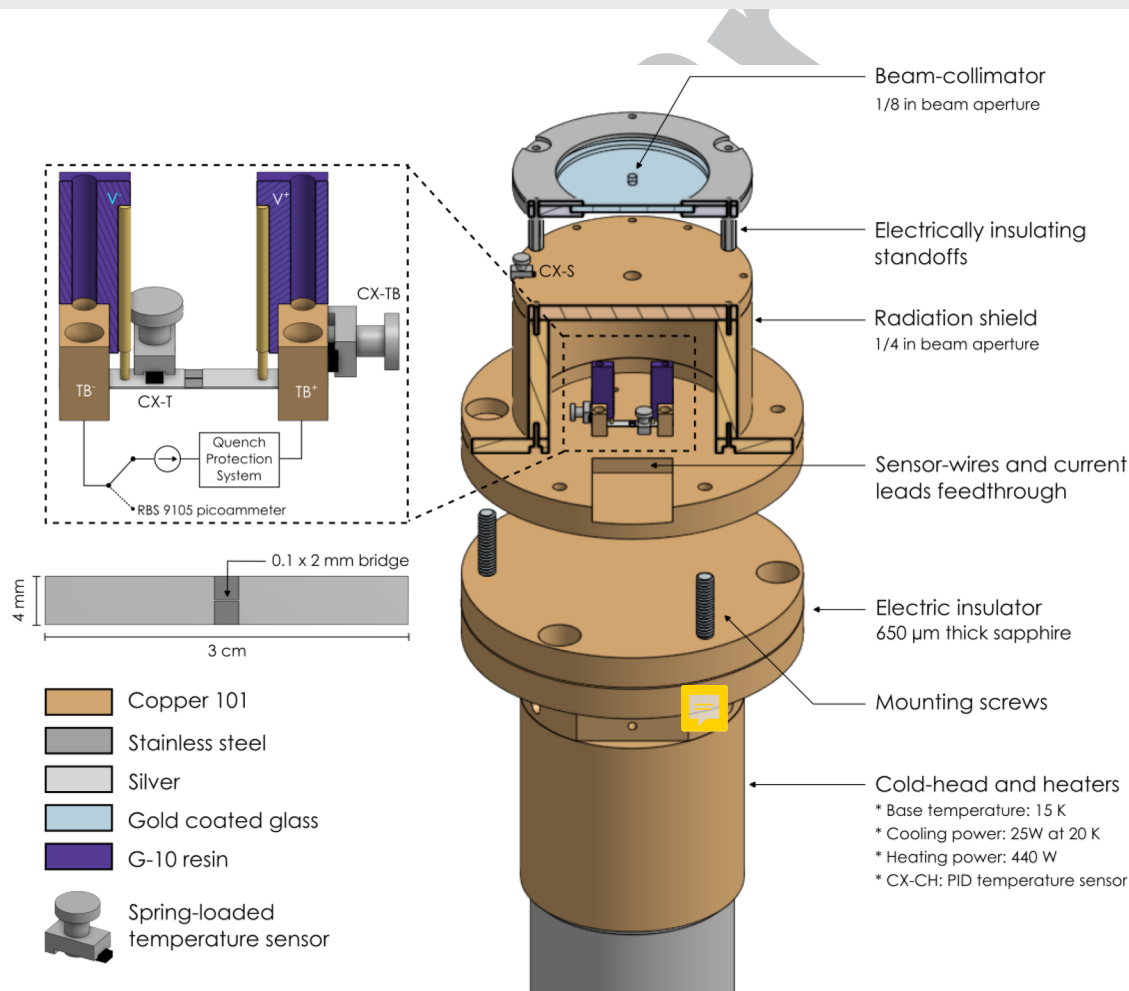
### 1. Irradiation target holder cryogenic design

The target holder is designed to maximize heat conduction while minimizing thermal radiation and Joule heating. Convective heat transfer between the cold mass and the chamber walls is largely suppressed by vacuum in the accelerator, where pressure remains under  $5 \times 10^{-6}$  Torr. The system is cooled from room temperature to 20 K in less than 2 h by a Cryomech AL-230 cold head, with 25 W of cooling power at 20 K and a base temperature of 15 K. Heating is provided by four parallel cartridge heaters, contributing a total of 400 W. The heaters are driven by a Sorenson DCS-150-7E power supply regulated by a LakeShore 336 temperature controller, which reads temperature from a sensor embedded in the cold head between the heaters (CX-CH). To maintain thermal contact through temperature cycles and compensate for different thermal contractions, all bolts are spring-loaded with Inconel 718 Belleville washers. Metal oxides are eliminated from all interfaces with solder flux and organic solvents, and the contact surfaces are lined with cryogenic grease. The N-Apiezon grease also minimizes the impact of surface roughness on heat conduction. A thin layer of indium ( $\sim 5 \mu\text{m}$ ) is preferred to grease where a fast thermal response (e.g., temperature sensors) or a good electrical connection (e.g., terminal blocks) is required. To avoid conducting heat from the feedthroughs to the tape, we use LakeShore Quad-Lead cryogenic wire (WQL-36) for Cernox sensors, twisted lead wire (WCT-34) for voltage probes, and AWG 12 copper wires for current leads soldered to the terminal blocks. All wires are also thermally anchored to the cold head.

A suite of three Cernox sensors is used to monitor the temperature of the target holder. The first is attached to the thermal shield (CX-S) and is used to quantify the radiative heat load. To minimize thermal radiation, the inner walls of the target chamber were covered with 24 sheets of multilayer insulation, except for the beam port and a 2-3/4" view-port used to image the beam fluorescence on the collimator. Any remaining thermal radiation is directly coupled to the heat sink by a radiation shield. The remaining heat load (either conducted by the cables or radiated by the shield) can



345 FIG. 2. The beamline and irradiation chamber of the cryogenic irradiation facility contain a set of diagnostics and actuators to maintain the intensity and spatial uniformity of  
346 the beam current. An upstream quadrupole magnet (not shown) is used to shape the beam, which can be imaged on the borosilicate glass collimator (by scintillation) and the  
347 beam profile monitor (by sampling charge).



348 FIG. 3. The cryogenic target assembly, made of copper and sapphire, (i) controls the sample temperature between 20 and 300 K; (ii) measures the superconducting properties  
349 of REBCO tapes during and after irradiation; and (iii) collects the beam current deposited on target as a measure of dose. The bridge pattern, engraved in the tape,  
350 reduces the current-limiting section of the tape to a 2  $\times$  0.1 mm segment.

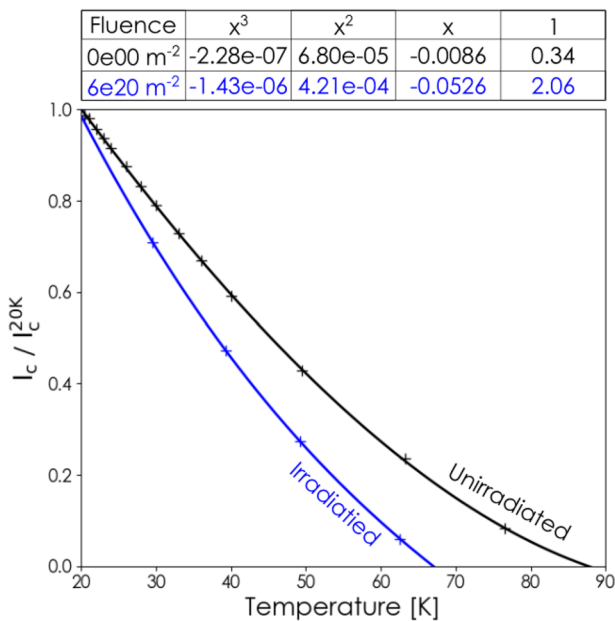


FIG. 4. In the 20–30 K range, a 0.4 K difference causes a 1% change in  $I_c$ . The sensitivity of  $I_c$  increases after irradiation, whereby a 1% change happens for a 0.3 K difference. The table provides the coefficients of a third-order polynomial fit. Each marker is the average of three measurements, and the error bars are smaller than the markers.

be inferred by the heating power required to maintain the temperature at 20 K compared to the nominal 25 W of cooling provided by the cold head.

The second Cernox sensor is affixed to the positive terminal block (CX-TB). This excludes any heat conducted by the current leads, e.g., poor thermal anchoring or Joule heating during transport measurements. If Joule heating is observed, the size of the current step is increased so that the system spends less time at high current. This ensures that the I–V curve is not distorted by a temperature increase.

With these provisions, sensor CX-TB agrees with sensor CX-T-pressed against the surface of the tape, ~4 mm away from the center of the beam spot—within their typical fluctuations ( $\pm 0.1$  K) over the range of 20–300 K. This bounds the temperature of REBCO and sets the maximum accuracy with which we can determine  $T_c$  and  $I_c$ . As shown in Fig. 4, a 0.4 K difference at about 20 K causes a 1% change in  $I_c$ . Sensors CX-TB and CX-T typically differ from CX-CH by less than 1 K, which is evidence for heat carried into the system by the current leads. A future upgrade of the facility thus foresees the use of superconducting current leads to eliminate Joule and conductive heat loads. The accuracy of CX-T is routinely cross-checked by comparing I–V curves measured in a bath of liquid nitrogen to those taken *in situ* at 77.3 K. The *ex situ* test station uses the same set of electronics and power supplies as the target holder and provides a quick check before mounting a sample to the target holder.

During experiments, we observed that the temperature of the tape (CX-T) rose and fell as we steered the beam on and off

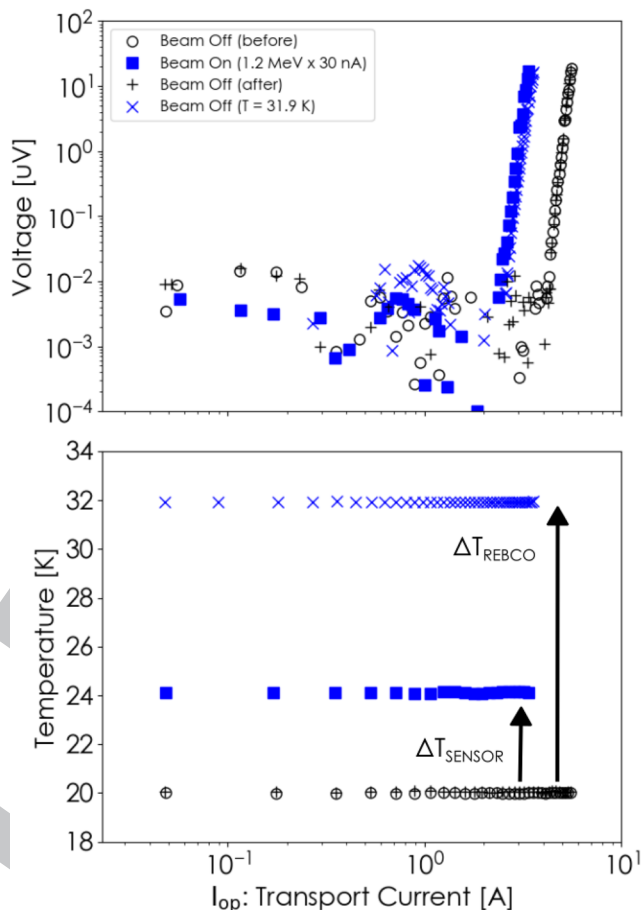


FIG. 5. The temperature needed to match the beam off curve (blue colored cross) to the beam on curve (blue colored square) suggests an 8 K gradient between the REBCO layer under irradiation ( $\Delta T_{REBCO}$ ) and temperature sensor CX-T ( $\Delta T_{SENSOR}$ ), located 4 mm away from the center of the beam spot.

the sample. This suggests ion beam heating but cannot be verified directly; adding a sensor in the irradiated area would block the beam. Therefore, we used the temperature dependence of  $I_c$ , obtained in thermal equilibrium without the beam, to infer the temperature of the REBCO layer during irradiation. This experiment, showcased in Fig. 5, points to an ~8 K gradient between the REBCO layer and the CX-T sensor for a 30 nA proton beam with an energy of 1.2 MeV. However, this conclusion is only valid if the suppression of  $I_c$ , measured during irradiation, is a predominantly thermal effect.

## 2. Online beam current measurements

Accurately quantifying dose requires a precise account of incident particles per unit area or fluence. Fluence is measured by tallying the charge deposited by the beam on the target holder with a picoammeter, connected to the positive terminal block by a relay. The RBD-950 picoammeter can measure beam currents with sub-nA resolution and provides a 90 V bias to prevent the loss of charge

408 caused by secondary electron emission when the beam hits the target.  
409 We find, however, that secondary electron suppression is not  
410 needed since the radiation shield acts as a Faraday cage for the elec-  
411 trons. For a homogeneous beam current density, the fluence is then  
412 a simple time integral of the beam current,

$$413 \Phi \left[ \frac{\text{protons}}{\text{m}^2} \right] = \frac{1}{Ze} \int dt I_b(t), \quad (2)$$

414 where  $I_b(t)$  is the ion beam current measured in nA,  $Z$  is the  
415 charge of the incident ion, and  $e$  is the elementary charge. For a  
416 1/8 in. diameter collimator,  $d$ , the constant preceding the integral  
417 is  $\sim 7.9 \times 10^{14}$  protons/nA m<sup>2</sup>.

418 Fluence measurements can provide an estimate of primary  
419 radiation damage, reported as the number of displacements per  
420 atom (dpa) in the irradiated volume. While dpa is a calculated quanti-  
421 ty that depends on a displacement model and does not consider  
422 the evolution of defects beyond the initial stages of the damage  
423 cascade, it is a necessary step to compare radiation effects across  
424 incident particle species and energies. The gold standard for dpa cal-  
425 culations is a Monte Carlo code known as the Stopping Range  
426 of Ions in Matter (SRIM), which implements the NRT model under  
427 the binary collision approximation.<sup>40</sup> However, SRIM has known  
428 (and often overlooked) issues and numerical artifacts. For example,  
429 the peaks and troughs featured at the layer boundaries in Fig. 1 are  
430 caused by the free-flight approximation, used in both Kinchin-Pease  
431 and Full Cascade calculations. The SRIM documentation suggests  
432 that “you do not worry about small peaks and dips at layer edges;  
433 they are not worth the trouble to try to avoid, and just average the  
434 final curves.”<sup>40</sup> However, in the case of coated conductors, these fea-  
435 tures are large, and it is not obvious that averaging would produce  
436 meaningful results. Instead, we repeated the calculation for 1.0 MeV  
437 protons impacting a pure YBCO target, accounting for the energy  
438 lost to the silver layer. The resulting “corrected” profile is compared  
439 to the full-tape calculation in Fig. 1, showing good agreement away  
440 from the layer boundaries and a linear slope that is consistent with  
441 uniform stopping power through a homogeneous material. A lesser-  
442 known issue is that the random seed of the Monte-Carlo simulation  
443 is only set once and repeats itself every 50k ions.<sup>41</sup> To obtain suf-  
444 ficient statistics (typically 300k ions and above for displacements),  
445 it was therefore necessary to restart the calculation periodically and  
446 average the results of several runs. Under these conditions, SRIM  
447 provides an average number of vacancies/Å-ion,  $K_{\text{SRIM}}$ , that can be  
448 used to convert from fluence to dpa,

$$449 [dpa] = \frac{K_{\text{SRIM}}}{N_{\text{YBCO}}} \Phi, \quad (3)$$

450 where  $N_{\text{YBCO}} \approx 7.5 \times 10^{28}$  atoms/m<sup>3</sup>, and  $K_{\text{SRIM}} = K_{\text{PKA}} + K_{\text{recoils}}$ ,  
451 calculated for 1.2 MeV protons incident on a Faraday Factory tape.  
452 This ratio is  $\sim 2.8 \times 10^{-24}$  using the Kinchin-Pease displacement  
453 model.

454 Repeatability is a common issue when comparing the results  
455 of irradiation experiments. Aside from sample-to-sample variations,  
456 discrepancies arise from spatial and temporal inhomogeneities in the  
457 ion-beam flux density. Such dose rate variations can confound irra-  
458 diation results in several ways. Inhomogeneous or slowly rastered  
459 beams can change the point-defect kinetics over the irradiated area,  
causing neighboring regions to evolve asynchronously.<sup>20</sup> In our

460 setup, the beam is shaped into a Gaussian profile with a FWHM  
461 equal to or larger than the 1/8 in. pinhole of the gold-coated glass  
462 collimator using a quadrupole and a beam-profile monitor. The  
463 gold coating is regularly refreshed to ensure that the accumulated  
464 charge can be exhausted through a grounding wire. Otherwise, arc-  
465 ing occurs, which can destabilize the beam, causing large variations  
466 in the beam current measured on the tape.

467 Inhomogeneous damage also happens as a function of depth.  
468 Since ions interact with lattice atoms by Coulomb scattering, the  
469 damage profile peaks where the ion has lost most of its energy. This  
470 region, known as the Bragg peak, is characterized by a steep gra-  
471 dient in dose rate and a large number of implanted interstitials.  
472 Torsello *et al.* showed that a shallow Bragg peak within the sub-  
473 strate can transfer a significant strain field to the superconducting  
474 layer and accelerate  $I_c$  degradation in iron-based superconductors.<sup>42</sup>  
475 Using 1.2 MeV protons, the Bragg peak is located several microns  
476 into the substrate and assumed to have a negligible effect on the  
477 REBCO layer (see Fig. 1). Experiments are underway to verify this  
478 assumption. A “deep” Bragg peak also limits the number of injected  
479 interstitials, which can change the chemistry of REBCO or stabilize  
480 voids in the case of H and He. By using a 1200 keV proton beam,  
481 less than 0.047% of the ions are deposited in the REBCO layer. In  
482 other words, for a dose of  $10^{20}$  protons/m<sup>2</sup>, there are  $\sim 0.25$  appm-H  
483 in REBCO.

### 3. In situ transport-current measurements

484 The four point probe arrangement used to measure  $I_c$  and  
485  $T_c$  is shown in the upper-left of Fig. 3. In this configuration, the  
486 tape is bolted to the base plate through terminal blocks (7/32 × 3/4  
487 × 3/8 in.<sup>3</sup>). Although the spring-loaded pins collect voltage *across*  
488 the entire tape, the voltage near  $I_c$  is almost exclusively caused by the  
489 current-limiting bridged section.

490 To determine  $I_c$ , the temperature is fixed while  $I_{\text{op}}$  (operating current)  
491 is increased. An IV measurement begins by stabilizing the  
492 sample temperature. Next, a thermal voltage offset is measured from  
493 the average of 20 values obtained at  $I_{\text{op}} = 0$  A. The current is then  
494 increased in small steps and measured by a Keithley DMM6500 dig-  
495 ital multimeter over a 1 mΩ shunt resistor. The voltage taps, labeled  
496 V+ and V- in Fig. 3, sample the voltage across the superconductor,  
497 which is digitized by a Keithley 2182A nanovoltmeter. The cur-  
498 rent ramp is terminated when the voltage reaches a predetermined  
499 threshold of up to 50 μV. Directly fitting the IV curve to Eq. (1), or a  
500 straight line on a log-log plot, yields  $I_c$  and the power law exponent  
501  $n$ . The latter procedure is known to lower the standard deviation  $\sigma$   
502 of repeated measurements. Most importantly,  $V_c > 2\delta V$ , meaning that  
503  $I_c$  is discernible from noise.

504 To determine  $T_c$ , the transport current is fixed while the tem-  
505 perature is increased. A measurement starts by stabilizing tempera-  
506 ture at a few Kelvin above, or below,  $T_c \approx 88$  K for the unirradiated  
507 tape, as shown in Fig. 6. The transport current is then fixed to 1  
508 mA, while temperature is slowly ramped across the superconduct-  
509 ing transition at a rate of 0.5 K/min. To exclude thermal voltages, we  
510 report the average of the voltage values measured with current flow-  
511 ing in the forward and reverse directions. The prescribed ramp rate  
512 offers a reasonable measurement time (10–20 min) and alignment  
513 between the upward-ramp and downward-ramp curves within the  
514 typical temperature fluctuation of CX-T, indicating that the REBCO  
515 temperature is in quasi-equilibrium. The simplest definition of  $T_c$  is  
516

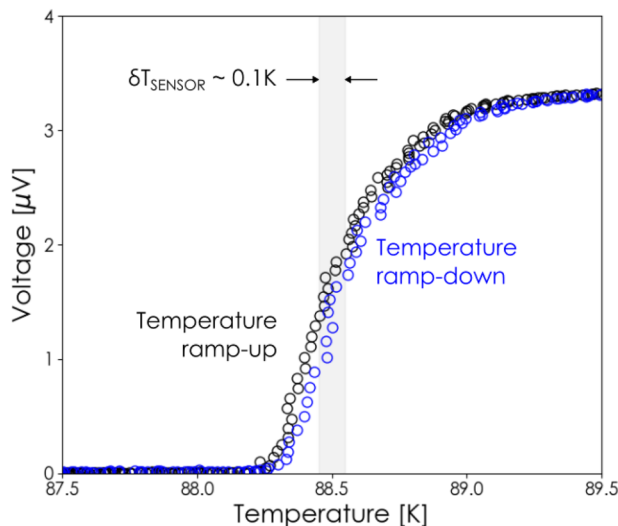


FIG. 6. Critical temperature measurement (0.5 K/min,  $I_{op} = 1$  mA) showing a typical temperature noise level  $\delta T < 0.1$  K, allowing measurements of  $T_c$  with the same precision.

517  
518  
519

520 given by the maximum of the first derivative of voltage with respect  
521 to temperature.

522

#### 4. Data acquisition and hardware control

523 The data acquisition and control (DAC) system is based on  
524 serial communication between a Linux desktop computer and  
525 the voltage, current, and temperature measurement devices. Two  
526 power supplies, also controlled by serial communication, run cur-  
527 rent through the tape. The first is a Lakeshore 121 Current Source  
528 ( $\pm 100$  nA up to 100 mA), used to measure  $T_c$ . The second is a Keith-  
529 ley 2231-A power supply that provides up to 6 A in steps as small  
530 as 1 mA. This power supply also provides a control voltage to an  
531 HP6260B current source that can provide up to 100 A in steps of  
532 0.3 A. Altogether, this system can apply transport currents from  
533 100 nA to 100 A, spanning nine orders of magnitude. The DAC  
534 is orchestrated by a custom-built PyQt5 graphical user interface  
535 (GUI) implementing the pySerial library to communicate with the  
536 serial ports. The temperature and tape-voltage signals are shielded  
537 by DB25 shielded-cables, from inside the target-holder to the mea-  
538 surement devices, where data are acquired at a rate of 3 points/s.  
539 In addition to reading voltage and temperature, the GUI provides  
540 remote control of vacuum pumps and cryocoolers using a Numato  
541 Lab 32 Channel USB Relay Module. Furthermore, the user can pre-  
542 define measurement sequences to run automated data acquisition  
543 routines. This software solution is complemented by a quench pro-  
544 tection system (QPS), a hardware fail-safe that can cut off the current  
545 supplied to the sample in  $\sim 1$  ms to avoid damage in the event of  
546 a quench. The QPS circuit consists of an instrumentation amplifier,  
547 low-pass and notch filters, and a window comparator. The compara-  
548 tor outputs a 12 V logic level into a D flip-flop, which activates the  
549 gate driver of a high-power transistor used to cut off the current. At  
550 the cutoff condition, the flip-flop is immediately cleared and remains  
551 in this state until the circuit is reset by the DAC. A schematic of the  
552 QPS is shown in Fig. 7.

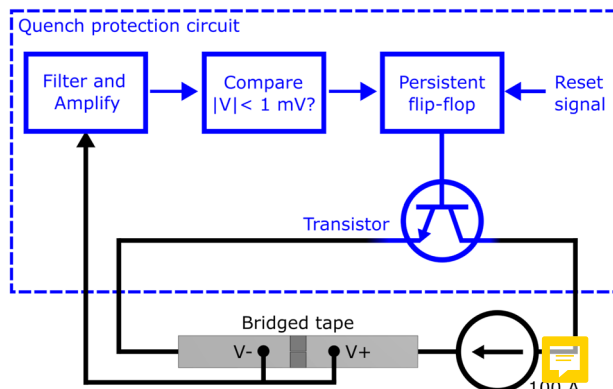


FIG. 7. Block diagram of the quench protection system, which can cut off the current supplied to the sample in  $\sim 1$  ms to avoid damaging the sample in case of a quench.

553  
554  
555

## IV. FIRST RESULTS

### A. Influence of irradiation temperature

Figure 8 shows preliminary results demonstrating the effect of different irradiation temperatures on  $I_c$ . Two pairs of REBCO tape samples were cut from the same spool and irradiated with 1.2 MeV protons, measuring  $I_c$  at 20 K after each fluence step. The flux was kept between 12 and  $15 \times 10^{16}$  protons/m<sup>2</sup>s, except for the tape plotted with open blue squares, where the dose rate was five times slower. The blue tapes, irradiated at 20 K, degrade significantly faster than their red counterparts, irradiated at 300 K. These data are compatible with the following explanation: at low temperatures, radiation-induced defects are frozen in place and preserved, while at high temperatures, thermal energy facilitates defect mobility and a larger fraction of Frenkel-pairs can recombine.

556  
557  
558  
559  
560  
561  
562  
563  
564  
565  
566  
567  
568  
569  
570

### B. Thermal annealing after cryogenic irradiation

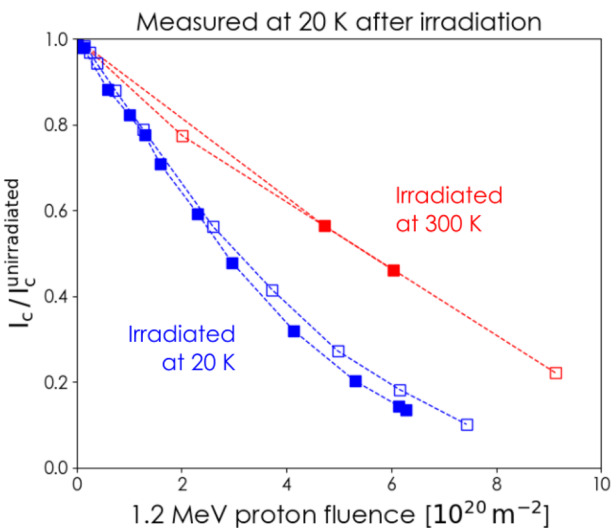
Figure 9 shows the evolution of  $I_c$  in a tape irradiated at 21 K, where the post-irradiation temperature is increased in steps of 3 K. For each step, the temperature is ramped at a rate of  $\sim 7$  K/min and held constant at the anneal temperature for 1 h. Each point is obtained by averaging eight measurements (taken at 21 K and 0 T). In this specific instance, where the tape had lost 8% of its unirradiated  $I_c$ , we found an onset of annealing effects at  $\sim 150$  K. Our facility also has the ability to investigate the time-dependence of annealing by sending millisecond pulses with amplitudes of several hundred amps. This causes Joule heating in the silver layer, warming the REBCO for very short periods of time.<sup>43</sup> Since thermal-cycles will occur during the maintenance of fusion and HEP devices, a better understanding of annealing mechanisms can be leveraged to maximize  $I_c$  recovery and, therefore, magnet lifetime.

571  
572  
573  
574  
575  
576  
577  
578  
579  
580  
581  
582  
583  
584  
585  
586

### C. Prompt suppression of $I_c$ during irradiation

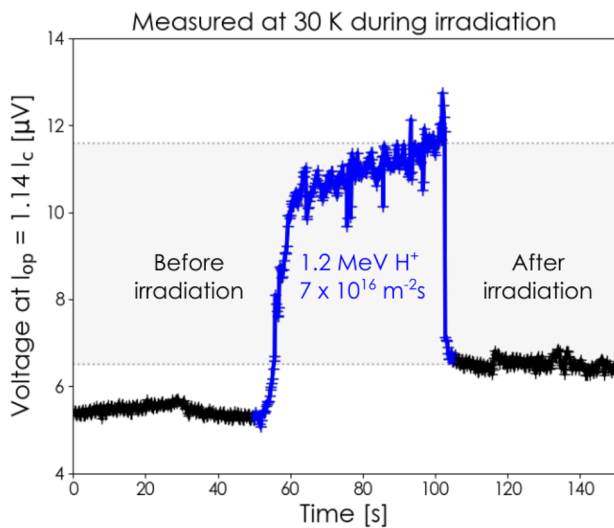
Finally, by applying transport current during irradiation, our facility can investigate the performance of REBCO in a radiation-field. For instance, Fig. 10 shows a significant increase in voltage

587  
588  
589  
590



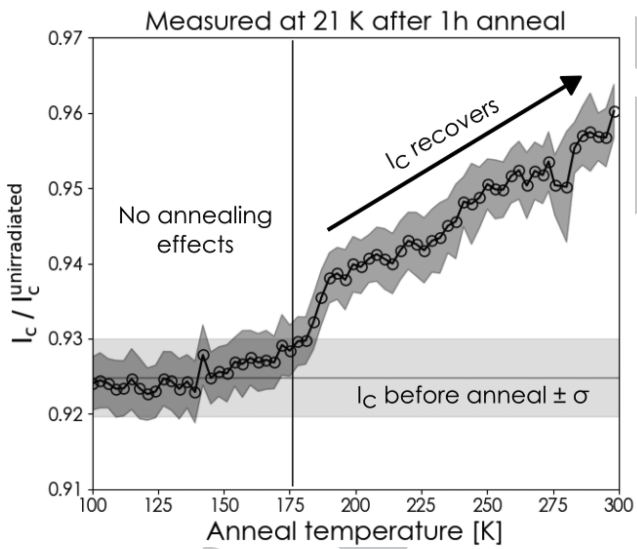
591  
592  
593  
594  
595  
596

**FIG. 8.** Cryogenic irradiation causes a faster degradation of  $I_c$  than room temperature irradiation since the defects are more mobile at 300 K than at 20 K and, therefore, recombine more easily. In this experiment, four identical samples were irradiated with 1.2 MeV protons at a typical flux density of  $12\text{--}15 \times 10^{16} \text{ m}^{-2}\text{s}$ . Each marker is the average of three measurements, and the error bars are smaller than the markers.



606  
607  
608  
609

**FIG. 10.** An instantaneous recovery of the critical current is observed when the beam is steered away from the sample, as indicated by an immediate drop in voltage. The higher baseline recorded after irradiation is likely due to the accumulation of stable defects.



597  
598  
599  
600

**FIG. 9.** Isochronal anneal steps carried out after irradiation at 21 K show that the critical current (21 K, 0 T) starts to recover well-below room temperature. In this figure, markers are the average of eight measurements with a standard deviation indicated by the envelope.

610  
611  
612  
613  
614  
615

at a fixed  $I_{\text{op}}/I_c = 1.14$ , which appears and disappears as the beam is steered on and off the sample. While ongoing research at MIT points to a predominant role of localized beam heating, alternative hypotheses have been proposed by the community to explain the beam-on effect. These include the breaking of Cooper pairs by

direct Coulombic interactions from the incident particle<sup>44</sup> or the large dynamic population of defects present during the ballistic stage of the damage cascade. Clarifying the extent to which beam heating can explain the beam suppression of  $I_c$  is important to determine if, e.g., a given flux of neutrons could perturb the steady-state operation of fusion magnets.

## V. FACILITY UPGRADES

616  
617  
618  
619  
620  
621  
622  
623  
624  
625  
626  
627  
628  
629  
630  
631  
632  
633  
634

Two efforts are presently underway to extend radiation damage studies of REBCO tapes at MIT and complement the capabilities of the cryogenic ion-irradiation facility.

The first extension is the planned addition of a compact, REBCO-based, split pair magnet providing *in situ*  $I_c(B, T, \theta)$  measurements at magnetic fields up to ~~10~~ T and magnetic-field-angles ranging from  $0^\circ$  to  $180^\circ$ . This upgrade will extend our critical measurements to the range where transport behavior is dominated by external magnetic fields and scaling laws can be used to confidently extrapolate our results to the high-field magnet performance range.<sup>45</sup> Another key objective of this upgrade is to further explore the impact of radiation damage on the  $I_c$  anisotropy regarding magnetic field direction. Previous *ex situ* results have shown that medium fluences degrade the  $B \parallel ab$  peak in  $I_c(\theta)$  and raise the  $B \parallel c$  levels, flattening the  $I_c(\theta)$  dependence and eliminating the anisotropic effects of strong external pinning centers used by REBCO manufacturers and exploited by magnet designers.<sup>35,46</sup>

635  
636  
637  
638  
639

The second extension is the construction of a new facility for cryogenic fast-neutron irradiation of magnet materials at the MIT Reactor (MITR-II), a 6 MW research reactor located on the main campus. The new facility targets relevant neutron fluences at cryogenic temperatures, with and without transport current, and with

in situ  $I_c(B, T, \theta)$  characterization. To achieve its target, the facility will make use of a unique capability of MITR-II known as a fast fission convertor, in which thermal neutron beams are incident on ex-core  $^{235}\text{U}$ , leading to fission and the emission of a Watt energy spectrum of neutrons that peaks around 1 MeV and extends up to  $\sim 8$  MeV. The fast neutrons are emitted into a cubic meter of atmospheric space adjacent to the reactor, in which the cryogenic irradiation facility will be built without the challenges of in-core engineering and with a larger experimental room where a 14 T Nb<sub>3</sub>Sn magnet will be installed for  $I_c(B, T, \theta)$  characterization. Importantly, the cryogenic irradiation of bulk magnet-relevant materials beyond REBCO, including other superconductors such as Bi2212 but also metals, insulation, solders, and instrumentation, is also planned for this facility, as are detailed proton-neutron irradiation similarity studies to better understand the radiation damage mechanisms and understand under what conditions proton irradiation can serve as a proxy for the more resource-intensive neutron irradiation.

## VI. CONCLUSION

A facility for the characterization of REBCO tapes under ion-irradiation is available at the MIT Plasma Science and Fusion Center. The *in situ* capability, i.e., cryogenic irradiation followed immediately by  $I_c$  measurement without an intermediate warm-up step, is essential to preserve the radiation-induced defect landscape within the REBCO layer and evaluate its consequences on the superconducting properties of the tape. Three demonstration measurements of REBCO tapes were presented: (1) the impact of irradiation temperature on the degradation of  $I_c$ ; (2) the onset temperature for annealing-recovery; and (3) the prompt suppression of  $I_c$ , which appears and disappears as the beam is steered on and off the sample. Each of these measurements carries new physical insights into the radiation tolerance of REBCO, and bears important consequences for the design and operation of large-scale magnets in fusion, HEP, and space applications. Combining the cryogenic ion-irradiation setup described in this paper with the upcoming cryogenic neutron irradiation facility will provide an unprecedented capability to study the behavior of REBCO tapes in radiation-intense applications. On the one-hand, ion-irradiations deliver rapid, low-cost, and experimentally flexible capabilities with a variety of species, energies, and *in situ* characterization techniques. Neutron irradiations, on the other hand, offer the highest fidelity irradiation and testing of REBCO tapes for fusion magnets. Both facilities are poised to deliver new scientific insights into cuprate superconductors, as well as better design criteria and operational certainty for large-scale REBCO magnets in the radiation field.

## ACKNOWLEDGMENTS

This work was supported by Eni S.p.A. through the MIT Energy Initiative. A.R.D. is grateful to Vadim Amelichev (S-Innovations) and Alexander Molodyk (Faraday Factory Japan) who kindly provided coated-conductor samples for our research; to J.L. Cheng for continued access to the laser-skiver at Commonwealth Fusion Systems; to Lauryn D. Kortman and Zoe L. Fisher for their help and dedication to maintaining and improving the facility; and to the

accelerator gods for blessing our target chamber with big bright beautiful beams during the experimental campaign of 2022–2023.

## AUTHOR DECLARATIONS

### Conflict of Interest

The authors have no conflicts to disclose.

## Author Contributions

**A. Devitre:** Conceptualization (equal); Data curation (equal); Formal analysis (equal); Investigation (equal); Methodology (equal); Resources (equal); Software (lead); Validation (equal); Visualization (lead); Writing – original draft (lead); Writing – review & editing (lead). **D. X. Fischer:** Conceptualization (equal); Data curation (equal); Formal analysis (equal); Investigation (equal); Methodology (equal); Resources (equal); Software (supporting); Validation (equal); Visualization (supporting); Writing – original draft (supporting); Writing – review & editing (supporting). **K. B. Woller:** Conceptualization (equal); Investigation (equal); Methodology (equal); Resources (equal); Supervision (supporting). **B. C. Clark:** Resources (supporting); Writing – original draft (supporting). **M. P. Short:** Conceptualization (equal); Formal analysis (supporting); Funding acquisition (supporting); Investigation (supporting); Methodology (supporting); Project administration (supporting); Resources (supporting); Supervision (equal); Validation (supporting); Writing – original draft (equal). **D. G. Whyte:** Conceptualization (equal); Formal analysis (supporting); Funding acquisition (lead); Investigation (equal); Methodology (supporting); Project administration (equal); Resources (supporting); Supervision (equal). **Z. S. Hartwig:** Conceptualization (equal); Data curation (supporting); Formal analysis (supporting); Funding acquisition (equal); Investigation (supporting); Methodology (equal); Project administration (equal); Resources (equal); Supervision (lead); Validation (supporting); Visualization (supporting); Writing – original draft (equal); Writing – review & editing (equal).

## DATA AVAILABILITY

The cryogenically irradiated REBCO tapes are available upon reasonable request to MPS. All the data needed to evaluate the conclusions in this paper can be accessed directly at the repository (<https://doi.org/10.5281/zenodo.11002961>).

## REFERENCES

- <sup>1</sup>A. Molodyk, S. Samoilovikov, A. Markelov, P. Degtyarenko, S. Lee, V. Petrykin, M. Gaifullin, A. Mankevich, A. Vavilov, B. Sorbom, J. Cheng, S. Garberg, L. Kesler, Z. Hartwig, S. Gavrilkin, A. Tsvetkov, T. Okada, S. Awaji, D. Abramov, A. Francis, G. Bradford, D. Larbalestier, C. Senatore, M. Bonura, A. E. Pantoja, S. C. Wimbush, N. M. Strickland, and A. Vasiliev, “Development and large volume production of extremely high current density YBa<sub>2</sub>Cu<sub>3</sub>O<sub>7</sub> superconducting wires for fusion,” *Sci. Rep.* **11**, 2084 (2021).
- <sup>2</sup>D. G. Whyte, J. Minervini, B. LaBombard, E. Marmar, L. Bromberg, and M. Greenwald, “Smaller and sooner: Exploiting high magnetic fields from new superconductors for a more attractive fusion energy development path,” *J. Fusion Energy* **35**, 41–53 (2016).

- 743 <sup>3</sup>A. J. Creely, M. J. Greenwald, S. B. Ballinger, D. Brunner, J. Canik, J. Doody,  
744 T. Fülöp, D. T. Garnier, R. Granetz, T. K. Gray *et al.*, "Overview of the SPARC  
745 tokamak," *J. Plasma Phys.* **86**, 865860502 (2020).
- 746 <sup>4</sup>A. Sykes, A. Costley, C. Windsor, O. Asunta, G. Brittles, P. Buxton, V. Chuyanov,  
747 J. Connor, M. Gryaznevich, B. Huang, J. Hugill, A. Kukushkin, D. Kingham, A.  
748 Langtry, S. McNamara, J. Morgan, P. Noonan, J. Ross, V. Shevchenko, R. Slade,  
749 and G. Smith, "Compact fusion energy based on the spherical tokamak," *Nucl.*  
750 *Fusion* **58**, 016039 (2017).
- 751 <sup>5</sup>J. Alonso, I. Calvo, D. Carralero, J. Velasco, J. García-Regaña, I. Palermo, and D.  
752 Rapisarda, "Physics design point of high-field stellarator reactors," *Nucl. Fusion*  
753 **62**, 036024 (2022).
- 754 <sup>6</sup>D. Endrizzi, J. Anderson, M. Brown, J. Egedal, B. Geiger, R. Harvey, M. Ialovega,  
755 J. Kirch, E. Peterson, Y. Petrov *et al.*, "Physics basis for the Wisconsin HTS  
756 axisymmetric mirror (WHAM)," *J. Plasma Phys.* **89**, 975890501 (2023).
- 757 <sup>7</sup>K. Ferrone, C. Willis, F. Guan, J. Ma, L. Peterson, and S. Kry, "A review of  
758 magnetic shielding technology for space radiation," *Radiation* **3**, 46–57 (2023).
- 759 <sup>8</sup>M. Evans and A. Ignatiev, "Using lunar superconducting magnetic energy storage  
760 (LSMES) for NASA Artemis program," in *Lunar Surface Innovation Consortium  
761 (LSIC): Low Temperature Sub-kW Power and Energy Storage for the Lunar Surface*  
762 (NASA Technical Management, 2022), pp. 1–2.
- 763 <sup>9</sup>B. Sorbom, J. Ball, T. Palmer, F. Mangiarotti, J. Sierchio, P. Bonoli, C. Kas-  
764 ten, D. Sutherland, H. Barnard, C. Haakonsen, J. Goh, C. Sung, and D. Whyte,  
765 "ARC: A compact, high-field, fusion nuclear science facility and demonstration  
766 power plant with demountable magnets," *Fusion Eng. Des.* **100**, 378–405  
767 (2015).
- 768 <sup>10</sup>L. Bottura, S. A. Gourlay, A. Yamamoto, and A. V. Zlobin, "Superconducting  
769 magnets for particle accelerators," *IEEE Trans. Nucl. Sci.* **63**, 751–776 (2016).
- 770 <sup>11</sup>B. W. R. Kleiner, *Superconductivity: An Introduction* (Wiley-VCH Verlag  
771 GmbH & Co. KGaA, 2016) Boschstr. 12, 69469 Weinheim, Germany.
- Q4 <sup>12</sup>■, *Handbook of Superconductivity: Fundamentals and Materials* (■, ■), Vol. 1.
- 772 <sup>13</sup>W. K. Kwok, U. Welp, A. Glatz, A. E. Koshelev, K. J. Kihlstrom, and G. W. Crab-  
773 tree, "Vortices in high-performance high-temperature superconductors," *Rep.  
774 Prog. Phys.* **79**, 116501 (2016).
- 775 <sup>14</sup>K. Tsuchiya, X. Wang, S. Fujita, A. Ichinose, K. Yamada, A. Terashima, and A.  
776 Kikuchi, "Superconducting properties of commercial REBCO-coated conductors  
777 with artificial pinning centers," *Supercond. Sci. Technol.* **34**, 105005 (2021).
- 778 <sup>15</sup>R. Unterrainer, D. X. Fischer, A. Lorenz, and M. Eisterer, "Recovering the  
779 performance of irradiated high-temperature superconductors for use in fusion  
780 magnets," *Supercond. Sci. Technol.* **35**, 04LT01 (2022).
- 781 <sup>16</sup>S. B. L. Chislett-McDonald, L. Bullock, A. Turner, F. Schoofs, Y. Dieudonne,  
782 and A. Reilly, "In-situ critical current measurements of REBCO coated conductors  
783 during gamma irradiation," *Supercond. Sci. Technol.* **36**, 095019 (2023).
- Q5 <sup>17</sup>S. Chromik, C. Camerlingo, M. Sojkova, V. Strbík, M. Talacko, I. Malka, I.  
784 Bar, G. Barelli, and G. Jung, "Low energy electron beam processing of YBCO thin  
785 films," *Appl. Surf. Sci.* **395**, 42–49 (2017); part of Special Issue: Progress in Applied  
786 Surface, Interface and Thin Film Science and Solar Renewable Energy News IV.
- 787 <sup>18</sup>D. X. Fischer, R. Prokopoc, J. Emhofer, and M. Eisterer, "The effect of fast neu-  
788 tron irradiation on the superconducting properties of REBCO coated conductors  
789 with and without artificial pinning centers," *Supercond. Sci. Technol.* **31**, 044006  
790 (2018).
- 791 <sup>19</sup>A. A. Soman, S. C. Wimbush, N. J. Long, M. W. Rupich, C. Notthoff, P. Kluth, J.  
792 Leveneur, J. Kennedy, and N. M. Strickland, "Reduced critical current anisotropy  
793 and improved critical current performance in a combined pinning landscape cre-  
794 ated by proton and silver irradiation," *IEEE Trans. Appl. Supercond.* **33**, 6600805  
795 (2023).
- 796 <sup>20</sup>G. S. Was, *Fundamentals of Radiation Materials Science* (Springer, 2016).
- 797 <sup>21</sup>M. Frischherz, M. Kirk, J. Farmer, L. Greenwood, and H. Weber, "Defect cas-  
798 cades produced by neutron irradiation in  $\text{YBa}_2\text{Cu}_3\text{O}_{7-\delta}$ ," *Physica C* **232**, 309–327  
799 (1994).
- 800 <sup>22</sup>Y. Linden, W. Iliffe, G. He, M. Danaie, D. Fischer, M. Eisterer, S. Speller,  
801 and C. Grovenor, "Analysing neutron radiation damage in  $\text{YBa}_2\text{Cu}_3\text{O}_{7-\delta}$   
802 high-temperature superconductor tapes," *J. Microsc.* **286**, 3–12 (2022).
- 803 <sup>23</sup>Y. Jiang, Z. Chen, Y. Han, P. Deb, H. Gao, S. Xie, P. Purohit, M. W. Tate, J. Park,  
804 S. M. Gruner, V. Elser, and D. A. Muller, "Electron ptychography of 2D materials  
805 to deep sub-ångström resolution," *Nature* **559**, 343–349 (2018).
- <sup>24</sup>R. J. Nicholls, S. Diaz-Moreno, W. Iliffe, Y. M. Linden, T. Mousavi, M. Aramini,  
805 M. Danaie, C. R. M. Grovenor, and S. C. Speller, "Understanding irradiation dam-  
806 age in high-temperature superconductors for fusion reactors using high resolution  
807 x-ray absorption spectroscopy," *Commun. Mater.* **3**, 52 (2022).
- <sup>25</sup>A. Yabuuchi, T. Ozaki, H. Sakane, H. Okazaki, H. Koshikawa, S. Yamamoto, and  
808 T. Yamaki, "Characterization of the effect of ion irradiation on industrially pro-  
809 duced  $\text{GdBa}_2\text{Cu}_3\text{O}_{7-\delta}$  superconducting tapes using a slow positron beam," *Appl.  
810 Phys. Express* **13**, 123004 (2020).
- <sup>26</sup>R. Auguste, M. O. Liedke, M. Butterling, B. P. Uberuaga, F. A. Selim,  
811 A. Wagner, and P. Hosemann, "In situ measurements of non-equilibrium  
812 positron state defects during He irradiation in Si," *J. Appl. Phys.* **133**, 185901  
813 (2023).
- <sup>27</sup>B. S. Brown, R. C. Birtcher, R. T. Kampwirth, and T. H. Blewitt, "Resistivity and  
814 measurements in low temperature irradiated  $\text{Nb}_3\text{Sn}$  and  $\text{Nb}_3\text{Ge}$ ," *J. Nucl. Mater.*  
815 **72**, 76–82 (1978).
- <sup>28</sup>P. A. Hahn and M. W. Guinan, "A cryogenic system for fusion neutron irradia-  
816 tion and in-situ measurements on superconductors," in *Advances in Cryogenic  
817 Engineering*, edited by R. W. Fast (Springer US, Boston, MA, 1988), pp. 639–646.
- <sup>29</sup>I. M. Ichiro Mukouda and Y. S. Yoshiharu Shimomura, "Effects of low-  
818 temperature neutron irradiation on  $T_c$  of  $\text{LnBa}_2\text{Cu}_3\text{O}_{7-y}$  ( $\text{Ln} = \text{Y}, \text{La}$ ) and  
819  $\text{La}_2\text{CuO}_4$ ," *Jpn. J. Appl. Phys.* **30**, 2744–2746 (1991).
- <sup>30</sup>H. Gerstenberg and W. Gläser, "Neutron irradiations at temperatures below 6 K  
820 at the munich research reactor (FRM)," *Nucl. Sci. Eng.* **110**, 50–55 (1992).
- <sup>31</sup>P. Müller, W. Schindler, G. Saemann-Ischenko, H. Burzlaff, H. Gerstenberg, and  
821 M. Fischer, "Neutron irradiation of  $\text{YBa}_2\text{Cu}_3\text{O}_7$  and  $\text{Y}_{1.2}\text{Ba}_{0.8}\text{CuO}_x$ ," *Physica C*  
822 **153–155**, 343–344 (1988).
- <sup>32</sup>S. A. Davydov, B. N. Goshchitskii, A. E. Karkin, A. V. Mirmelshtein, V. I.  
823 Voronin, M. V. Sadovskii, V. L. Kozhevnikov, S. V. Verkhovskii, and S. M. Chesh-  
824 nitskii, in *Advances in Superconductivity*, edited by K. Kitazawa and T. Ishiguro  
825 (Springer Japan, 1989), Vol. 1, pp. 463–468.
- <sup>33</sup>H. Wiesinger, F. Sauerzopf, H. Weber, H. Gerstenberg, and G. Crabtree,  
826 "Flux pinning by collision cascades and large defect clusters in single crystal  
827  $\text{YBa}_2\text{Cu}_3\text{O}_{7-\delta}$ ," *Europhys. Lett.* **20**, 541 (1992).
- <sup>34</sup>B. Egner, J. Geerk, H. C. Li, G. Linker, O. Meyer, and B. Strehlau, "The influence  
828 of irradiation-induced defects on the superconductivity of  $\text{YBa}_2\text{Cu}_3\text{O}_7$ ," *Jpn. J.  
829 Appl. Phys.* **26**, 2141 (1987).
- <sup>35</sup>B. N. Sorbom, "The effect of irradiation temperature on REBCO  $J_c$  degradation  
830 and implications for fusion magnets," Ph.D. thesis, Massachusetts Institute of  
831 Technology, 2017.
- <sup>36</sup>W. Iliffe, N. Peng, G. Brittles, R. Bateman, R. Webb, C. Grovenor, and S.  
832 Speller, "In-situ measurements of the effect of radiation damage on the supercon-  
833 ducting properties of coated conductors," *Supercond. Sci. Technol.* **34**, 09LT01  
834 (2021).
- <sup>37</sup>S. R. Folty, L. Civale, J. L. Macmanus-Driscoll, Q. X. Jia, B. Maiorov,  
835 H. Wang, and M. Maley, "Materials science challenges for high-temperature  
836 superconducting wire," *Nat. Mater.* **6**, 631–642 (2007).
- <sup>38</sup>T. Benkel, Y. Miyoshi, X. Chaud, A. Badel, and P. Tixador, "REBCO tape  
837 performance under high magnetic field," *Eur. Phys. J. Appl. Phys.* **79**, 30601  
838 (2017).
- <sup>39</sup>K. Tang, "Evaluation of novel laser-skived microbridges for improved char-  
839 acterization of REBCO superconductor," Master's thesis, Massachusetts Institute of  
840 Technology, 2023.
- <sup>40</sup>J. F. Ziegler, M. Ziegler, and J. Biersack, "SRIM—The stopping and range of ions  
841 in matter (2010)," *Nucl. Instrum. Methods Phys. Res., Sect. B* **268**, 1818–1823  
842 (2010), a part of Special Issue: 19th International Conference on Ion Beam  
843 Analysis.
- <sup>41</sup>M. Short, D. Gaston, M. Jin, L. Shao, and F. Garner, "Modeling injected inter-  
844 stitial effects on void swelling in self-ion irradiation experiments," *J. Nucl. Mater.*  
845 **471**, 200–207 (2016).
- <sup>42</sup>D. Torsello, M. Fracasso, R. Gerbaldo, G. Ghigo, F. Laviano, A. Napolitano, M.  
846 Iebole, M. Cialone, N. Manca, A. Martinelli, L. Piperno, V. Braccini, A. Leo, G.  
847 Grimaldi, A. Vannozzi, G. Celentano, M. Putti, and L. Gozzelino, "Proton irra-  
848 diation effects on the superconducting properties of Fe(Se,Te) thin films," *IEEE  
849 Trans. Appl. Supercond.* **32**, 7500105 (2022).

- 865      <sup>43</sup>Z. L. Fisher, "Annealing cryogenically irradiated high temperature super-  
866      conductors with current pulses," Master's thesis, Massachusetts Institute of  
867      Technology, 2023.  
868      <sup>44</sup>W. Iliffe, K. Adams, N. Peng, G. Brittles, R. Bateman, A. Reilly, C. Grovenor, and  
869      S. Speller, "The effect of *in situ* irradiation on the superconducting performance  
870      of REBa<sub>2</sub>Cu<sub>3</sub>O<sub>7-δ</sub>-coated conductors," *MRS Bull.* **48**, 710 (2023).

- 871      <sup>45</sup>C. Senatore, C. Barth, M. Bonura, M. Kulich, and G. Mondonico, "Field and  
872      temperature scaling of the critical current density in commercial REBCO coated  
873      conductors," *Supercond. Sci. Technol.* **29**, 014002 (2015).  
874      <sup>46</sup>N. M. Strickland, S. C. Wimbush, A. A. Soman, P. Kluth, C. Notthoff, R. Knibbe,  
875      M. Li, and M. W. Rupich, "Isotropic and anisotropic flux pinning induced by  
876      heavy-ion irradiation," *IEEE Trans. Appl. Supercond.* **32**, 8000505 (2022).

Author Proof